universe

MDPI

Article

Interacting Dark-Sector Models with Bulk Viscosity Under Dynamical Stability and Observational Constraints

Cristofher Z. Vargas *, William C. Algoner *, Angel E. Obispo and Andrés G. Jirón

Facultad de Ingeniería, Universidad Tecnológica del Perú, Av. Tacna y Arica 160, Arequipa 04001, Peru; aobispo@utp.edu.pe (A.E.O.); ajiron@utp.edu.pe (A.G.J.)

* Correspondence: crzuniga@utp.edu.pe (C.Z.V.); e19938@utp.edu.pe (W.C.A.)

Abstract

Although the standard model of cosmology (ΛCDM) has been successful in explaining a wide range of observational phenomena, it still faces significant limitations, particularly regarding the nature and properties of the dark sector of the universe. These challenges motivate the exploration of alternative approaches that can deepen our understanding of cosmic evolution. This study proposes an extension of the ΛCDM model by incorporating irreversible processes through a viscous fluid with out of equilibrium pressure. This fluid interacts dynamically with the dark sector components, offering new possibilities for describing the expansion of the universe. To constrain the proposed scenarios, we perform a Bayesian statistical analysis using the Pantheon+ Type Ia supernova compilation, Cosmic Chronometers, and DESI DR2 Baryon Acoustic Oscillation measurements. The observational results show that all three interaction models successfully reproduce the late-time expansion history while preserving a dark matter barotropic index close to the pressureless limit expected in the standard cosmological scenario. In contrast, the dark energy barotropic index consistently favors positive values, suggesting a mild departure from the cosmological constant description. The incorporation of Cosmic Chronometers and, particularly, BAO measurements substantially improves the constraints on the matter sector, leading to a significant reduction in the uncertainty of the present dark matter density parameter, whereas the bulk-viscosity parameter and the asymptotic ratio remain only weakly constrained. Finally, a Bayesian model comparison based on the Bayes factor shows that the interacting dissipative models remain observationally compatible with the reference ΛCDM cosmology. According to the Jeffreys scale, the resulting Bayesian evidence is inconclusive, indicating that current observations neither favor nor disfavor these extensions with respect to the standard cosmological model.

Keywords: dissipative cosmology; dark sector interaction; bulk viscosity; dynamical stability; stationary solutions; ΛCDM extension

Check for updates

Academic Editor: Júlio César Fabris

Received: 16 February 2026
Revised: 13 July 2026
Accepted: 21 July 2026
Published: 10 August 2026

Copyright: © 2026 by the authors. Licensee MDPI, Basel, Switzerland. This article is an open access article distributed under the terms and conditions of the Creative Commons Attribution (CC BY) license.

1. Introduction

Modern cosmology describes the large-scale evolution of the universe using a model based on a homogeneous and isotropic space-time governed by the Friedmann Equations. In this context, the dynamics of cosmology are primarily governed by an energy composition consisting of two enigmatic components, dark matter and dark energy, the physical nature of which remains unknown to date. Observational evidence supporting this scenario has been derived from type Ia supernovae, baryon acoustic oscillations, anisotropies in the cosmic microwave background, and direct measurements of the expansion parameter [1–4].

These data suggest that the Universe is in a phase of accelerated expansion, dominated by a component with negative pressure, whereas structure formation requires an additional non-relativistic component. Despite the success of the standard cosmological model in describing the background, its underlying formulation does not provide a physical explanation for the origin or the dynamics of the dark components. In recent years, the joint analysis of early- and late-time observations has revealed persistent discrepancies in the estimation of certain cosmological parameters, particularly the current value of the Hubble constant [5–9]. Estimates derived from the cosmic microwave background differ from those obtained from Type Ia Supernovae, Cosmic Chronometers, and Baryon Acoustic Oscillations [1,10–13]. These differences have motivated the investigation of extensions to the standard cosmological model that preserve cosmological symmetry but allow for more general dynamics in the energy sector. In this context, models that incorporate effective interactions between dark matter and dark energy or dissipative processes at the macroscopic level have been widely explored as consistent phenomenological alternatives.

The interaction models in the dark sector modify the individual conservation Equations, allowing energy exchange between dark matter and dark energy while preserving the total conservation. This approach has been used to study the evolution of the ratio between dark densities and to analyze the existence of asymptotic solutions different from the non-interacting scenario [14–17]. From a dynamical perspective, these models make it possible to investigate the conditions under which the ratio between densities evolves toward a constant value at late times, which is related to the cosmological coincidence problem. Recent studies show that, when interacting models are confronted with late time expansion data, the background dynamics generally remain close to those of the standard model, which motivates the use of additional dynamical criteria to distinguish between different scenarios [18–21].

In parallel, a line of research has been developed focusing on the inclusion of dissipative processes in cosmology through a nonequilibrium pressure associated with bulk viscosity. In this approach, the effective pressure of the cosmological fluid is modified by a term proportional to the expansion parameter, which represents a macroscopic description of irreversible processes or deviations from thermodynamic equilibrium [22–24]. At the cosmological background level, bulk viscosity can influence the late-time expansion and asymptotic behavior of the universe without introducing new fundamental components. This type of model has been used to study cosmic acceleration, thermodynamic properties, and observational constraints [25–27].

A relevant framework that combines interaction in the dark sector and effective dissipation was developed by Kremer and Sobreiro, who proposed a cosmological model with interacting dark fluids and non-equilibrium pressure within a Friedmann–Robertson–Walker description [28]. In this approach, bulk viscosity is explicitly introduced through an additional pressure proportional to the expansion parameter, and the energy exchange between the dark components is incorporated in a consistent manner. This treatment provides a suitable basis for studying dissipative cosmological models and has served as a foundation for the developments that followed.

On the other hand, Chimento, Forte, and Kremer introduced an effective framework for characterizing interactions within the dark sector by utilizing effective barotropic indices [29]. This approach encodes the interaction through a function of the density ratio, which modifies the effective barotropic index of the dark energy. Such parameterization results in an autonomous Equation governing the evolution of the density ratio, thereby facilitating the establishment of general stability conditions for stationary solutions. This method obviates the necessity of explicitly incorporating an interaction term into the conservation Equations, allowing the analysis of the system dynamics based on global

properties. The methodology proposed in their study serves as the conceptual foundation for the present study.

In recent years, numerous studies have revisited models of interaction and dissipation, driven by both observational discrepancies and the necessity to explore controlled extensions of the standard model [30–34]. Notably, the use of modern datasets, such as Pantheon+, BAO measurements from spectroscopic surveys, cosmic chronometers, and CMB, has enabled a broader assessment of the expansion history and the acoustic scale [1,11,35,36].

In this study, the effective barotropic index approach proposed by Chimento and collaborators is adopted, in combination with the inclusion of a non-equilibrium pressure associated with bulk viscosity, following the methodology developed by Kremer. A flat universe is considered, with baryons, photons, and neutrinos included in the background evolution, while the dark sector is composed of dark matter and dark energy. The interaction is introduced through a function of the density ratio that modifies the effective barotropic index of dark energy and leads to an autonomous Equation for the evolution of the ratio. On this basis, three functional forms of interaction are proposed that satisfy stability conditions and allow for analytical solutions for the cosmological dynamics. The models are confronted with current observational data, including SNIa, CC, and BAO data, with the aim of evaluating their compatibility with modern cosmological constraints [27,35,37,38].

The paper is organized as follows. In Section 2, the dissipative cosmological framework is presented, adopting the effective barotropic index approach and incorporating a non-equilibrium pressure associated with bulk viscosity, together with photon and neutrino contributions. In Section 3, the interaction function $F(r)$ is introduced, and three functional forms are proposed, corresponding to Models 1–3. In Section 4, the statistical analysis and observational constraints are described, including SNIa, CC, and BAO data. In Section 5, the results are presented and discussed. Finally, Section 6 summarizes the main conclusions.

2. Dissipative Cosmological Model

The model under consideration describes a universe composed of a mixture of dark energy (de), photons (γ), neutrinos (ν) and a matter field (m), the latter consisting of baryonic matter (b) and dark matter (dm). In addition, irreversible processes in cosmic evolution are incorporated by including a non-equilibrium pressure. The main equations of this model are presented in [28], and for completeness, they are briefly described below.

First, a spatially flat Friedmann–Lemaître-Robertson–Walker metric is considered,

$$ds^2 = dt^2 - a(t)^2\,(dx^2 + dy^2 + dz^2), \tag{1}$$

where $a(t)$ denotes the cosmic scale factor to describe a homogeneous and isotropic universe. If $\rho = \rho_m + \rho_\gamma + \rho_\nu + \rho_{de}$ and $P = P_m + P_\gamma + P_\nu + P_{de}$ represent the total energy density and total pressure, respectively, the Friedmann equation and the energy-density evolution equations are given by

$$\left(\frac{\dot{a}}{a}\right)^2 = \frac{8\pi G}{3}(\rho_b + \rho_{dm} + \rho_\gamma + \rho_\nu + \rho_{de}), \tag{2}$$

$$\dot{\rho}_b + 3\left(\frac{\dot{a}}{a}\right)\rho_b = 0, \tag{3}$$

$$\dot{\rho}_\gamma + 4\left(\frac{\dot{a}}{a}\right)\rho_\gamma = 0, \tag{4}$$

$$\dot{\rho}_\nu + 3\left(\frac{\dot{a}}{a}\right)\left[1 + \frac{1}{3}\left(\frac{1}{1+(\frac{a}{a_{nr}})^2}\right)\right]\rho_\nu = 0, \tag{5}$$

$$\dot{\rho}_{dm} + \dot{\rho}_{de} + 3\left(\frac{\dot{a}}{a}\right)(\rho_{dm} + P_{dm} + \rho_{de} + P_{de} + \varpi) = 0, \tag{6}$$

where the dot represents time derivative, the quantity a_{nr} corresponds to the cosmic scale factor when neutrinos become non-relativistic (see Appendix B of Ref. [39] for further details) and ϖ is the non-equilibrium pressure. According to [29], Equation (6) can be decomposed into two effective conservation equations

$$\dot{\rho}_{dm} + 3\left(\frac{\dot{a}}{a}\right)\gamma^e_{dm}\rho_{dm} = 0, \tag{7}$$

$$\dot{\rho}_{de} + 3\left(\frac{\dot{a}}{a}\right)\gamma^e_{de}\rho_{de} = 0, \tag{8}$$

with γ^e_i and $(i = dm, de)$ denoting effective barotropic indeces. The effective barotropic indices are connected to each other by

$$\gamma^e_{dm} = \gamma_{dm} + \frac{\gamma_{de} - \gamma^e_{de}}{r} + \frac{\varpi}{\rho_{dm}}, \tag{9}$$

where $\gamma_i, (i = dm, de)$ are constant barotropic indices associated with the equations of state $P_i = (\gamma_i - 1)\rho_i$ and $r \equiv \rho_{dm}/\rho_{de}$ denotes the ratio of energy densities. In cosmological models that incorporate dissipative processes, cosmic expansion can drive the system away from thermodynamic equilibrium. In this context, bulk viscosity can be interpreted as an effective macroscopic manifestation of irreversible processes occurring during cosmological expansion. Several physical mechanisms have been proposed in the literature as possible origins of viscous effects in the dark sector, including self-interacting dark matter, particle production processes, kinetic nonequilibrium phenomena, and coarse-grained descriptions of unknown microphysics [40,41]. These mechanisms may generate entropy production and effective negative pressure contributions during the expansion of the Universe. Therefore, the viscous pressure introduced in the present work is treated phenomenologically as an effective contribution encoding deviations from local thermodynamic equilibrium rather than as the consequence of a specific microscopic model [42,43]. Such departures are modeled through a non-equilibrium pressure, which in the first-order relativistic formalism is written as $\varpi = -3\eta\dot{a}/a$. This relation indicates that dissipation is directly associated with accelerated expansion and that the viscous term introduces an effective negative contribution to the total pressure of the fluid. To characterize viscosity without introducing additional fields while retaining a physically motivated dependence, the viscosity coefficient η is assumed to be linked to the dark matter sector. Specifically, the Ansatz $\eta = \eta_0 \frac{\rho_{dm}\sqrt{\rho}}{H^2}$ is adopted, where η_0 is a dimensionless parameter that controls the intensity of the dissipative effect, ρ_{dm} is the dark matter energy density, ρ is the total energy density, and H is the Hubble parameter. This functional form allows viscous effects to become relevant at late times, when dark matter dominates the non-relativistic sector, and yields an effective pressure capable of altering the evolution of the matter to dark energy density ratio and the overall dynamics of the model, without modifying the fundamental structure of the cosmological equations.

An interaction between dark matter and dark energy is physically admissible because general relativity requires only the conservation of the total cosmic fluid, whereas the individual dark components are not necessarily conserved separately. From this perspective, the dark sector may allow an effective transfer of energy between dark matter and dark energy without violating the global conservation equation. Interacting dark-sector models

have been extensively explored as phenomenological extensions of ΛCDM and may be related to coupled scalar fields or other unknown physical processes beyond the standard cosmological scenario. In this work, the function $F(r)$ is introduced phenomenologically to encode the possible energy exchange between the dark components through the density ratio $r \equiv \rho_{dm}/\rho_{de}$.

Following [29], the effective dark energy barotropic index is defined as $\gamma_{de}^{e} = \gamma_{de} - F(r)$, where the general function $F(r)$ encodes the interaction between the dark fluids. Combining Equations (7) and (8), the evolution equation for r is obtained as

$$\dot{r} = -3\frac{\dot{a}}{a} r \left[\gamma_{dm} - \gamma_{de} + \left(1 + \frac{1}{r}\right) F(r) - \bar{\eta}_0 \right] \tag{10}$$

where $\bar{\eta}_0 = \sqrt{\frac{27}{8\pi G}}\eta_0$. Solutions yielding an explicit dependence of the energy densities ρ_{dm} and ρ_{de} on the cosmic scale factor a are sought using the evolution Equations (7), (8) and (10). Because the barotropic indices γ_{dm} and γ_{de} are taken to be constants, an explicit specification of $F(r)$ as a function of r is required. Under this assumption, the bracketed term depends only on r, so Equation (10) can be rewritten as

$$\dot{r} = -3Hr\mathcal{F}(r) \tag{11}$$

where

$$\mathcal{F}(r) \quad = \quad \gamma_{dm} - \gamma_{de} + \left(1 + \frac{1}{r}\right) F(r) - \bar{\eta}_0. \tag{12}$$

The solution of the dynamical Equation (11) for r requires the specification of $F(r)$. Following [29], the admissible forms of $F(r)$ are constrained by a stability analysis of the energy density ratio r. The stationary state of the universe is characterized by a constant solution $r = r_s$. Therefore, Equation (11) implies $\mathcal{F}(r_s) = 0$, and the stationary solution is asymptotically stable provided that $\frac{d\mathcal{F}(r)}{dr}\Big|_{r=r_s} > 0$. This condition leads to

$$r(r+1)\frac{dF(r)}{dr} - F(r) > 0. \tag{13}$$

3. $F(r)$ Functions

The evolution of the ratio between dark matter and dark energy densities, $r \equiv \rho_{dm}/\rho_{de}$, is essential for characterizing the dynamics of the dark sector in the presence of both interaction and dissipative processes. In this context, the equation governing $\dot{r}$, which involves the barotropic difference $\gamma_{dm} - \gamma_{de}$, viscous term proportional to $\bar{\eta}_0$, and coupling term by $F(r)$, is given by Equation (10). Starting from this full expression, the dynamics can be rearranged into the autonomous form shown in Equation (11), allowing the combined effects of interaction, viscosity, and barotropic indices to be encapsulated in the function $\mathcal{F}(r)$.

The structural relation between the dynamical function $\mathcal{F}(r)$ and the physical interaction function $F(r)$, introduced in [29] through the modification of the effective barotropic index $\gamma_{de}^{e} = \gamma_{de} - F(r)$, is given by Equation (12). This equation specifies how γ_{dm}, γ_{de}, $\bar{\eta}_0$, and $F(r)$ combine to determine the functional form of the autonomous term, $\mathcal{F}(r)$. Accordingly, a stationary state [28] is characterized by the condition $\mathcal{F}(r_\infty) = 0$, which fixes the asymptotic value of the ratio between the matter and dark energy densities. The dynamical stability of this fixed point is governed by the asymptotic criterion given in Equation (13). Based on this condition and the functional structure imposed by Equation (12), physically consistent models must satisfy the following fundamental constraints

$$\gamma_{dm} > \gamma_{de} + \bar{\eta}_0, \quad r_\infty > 0. \tag{14}$$

These two conditions are not just formal constraints; they are essential for physical consistency. The first ensures that the effective difference between the barotropic indices dominates the viscous contribution, so that the dynamics neither reverse nor become divergent. The second condition ensures that in the late-time regime, the universe maintains a finite fraction of dark matter relative to dark energy, thereby ruling out unphysical solutions such as $r_\infty < 0$. These conditions are essential for constructing physically consistent models. Within this framework, models are uniquely specified by the choice of the interaction function $F(r)$, which determines the explicit analytical form of $r(a)$, dictates the convergence toward r_∞, and sets the functional dependence of the Hubble parameter $H(r)$. Therefore, the selection of the three models aims to identify distinct regimes of energy transfer within the dark sector that align with the autonomous structure in Equation (11), the algebraic relation in Equation (12), and the stability criterion in Equation (13). Each model, therefore, represents a different family of dissipative cosmological scenarios, all rooted in the same dynamical framework.

The three forms of $F(r)$ considered in this study should be viewed as phenomenological parameterizations of the interaction in the dark sector. They are constructed such that the stationary condition and stability criterion are satisfied while still allowing analytical solutions for cosmological dynamics. Therefore, these functions are not intended to describe a unique microscopic interaction mechanism but rather to provide simple and physically consistent scenarios for studying possible energy transfer effects between dark matter and dark energy.

3.1. Model 1

In this first scenario, a constant interaction is considered. In interacting dark-sector models, the function $F(r)$ acts as an effective term governing the energy exchange between dark matter and dark energy [29]. When the system is assumed to admit a stationary state $r = r_\infty$, the condition $\mathcal{F}(r_\infty) = 0$, obtained directly from Equation (11), naturally selects a constant interaction. This choice is also consistent with previously studied viscous models [28], where dissipative processes lead to a constant effective barotropic index. In this model, the structural relation given in Equation (12) determines the value of the asymptotic interaction as

$$F(r) \equiv F_\infty = -\frac{r_\infty}{1 + r_\infty}(\gamma_{dm} - \gamma_{de} - \bar{\eta}_0). \tag{15}$$

This expression guarantees that the stability condition given in Equation (13) is satisfied whenever the criterion in Equation (14) holds. These constraints prevent divergences in the dynamics and ensure that the late-time regime admits a physically acceptable fixed point. By substituting the constant interaction term in Equation (15) into Equation (10), the solution for the density ratio is given by

$$r = r_\infty + (r_0 - r_\infty) a^{-3\frac{\gamma_{dm} - \gamma_{de} - \bar{\eta}_0}{1 + r_\infty}}, \tag{16}$$

where r_0 denotes the ratio of the dark sector energy densities at the present time t_0. The corresponding ratio between baryonic matter and dark matter evolves as

$$\frac{\rho_b(a)}{\rho_{dm}(a)} = \frac{\Omega_{b_0}}{\Omega_{de_0}} \frac{a^{-3(1-\gamma_{de}+F_\infty)}}{\left(r_\infty + \left(r_0 - r_\infty\right) a^{-\frac{3(\gamma_{dm} - \gamma_{de} - \bar{\eta}_0)}{1 + r_\infty}}\right)}, \tag{17}$$

showing explicitly how the interaction in the dark sector modifies the relative abundance of dark matter with respect to baryons during the cosmological evolution. By solving Equations (6) and (8) and substituting the result into Equation (2), the Hubble parameter is obtained as

$$\frac{H^2}{H_0^2} = \Omega_{de_0}(1+r)a^{-3(\gamma_{de}-F_\infty)} + \Omega_{b_0}a^{-3} + \Omega_{\gamma_0}a^{-4} + \Omega_{\nu_0}a^{-4}\sqrt{1+(\frac{a}{a_{nr}})^2}, \tag{18}$$

where Ω_{de}, Ω_{γ_0}, Ω_{ν_0} and Ω_{b_0} are the parameters for dark energy density, photons, neutrinos and baryons, and H_0 is the Hubble constant.

3.2. Model 2

In this second scenario, the interaction function $F(r)$ is allowed to vary with the density ratio, thereby introducing a redshift dependent energy exchange between dark matter and dark energy. The functional form is constructed so that the stationary state coincides with that of Model 1, namely $F(r_\infty) = F_\infty$, while also satisfying the structural relation given in Equation (12), and the stability condition stated in Equation (13). Under these requirements, the interaction is chosen as

$$F(r) = \frac{1+r_\infty}{1+r}F_\infty\,, \tag{19}$$

which smoothly interpolates between a stronger interaction at early times ($r \gg r_\infty$) and the constant asymptotic value F_∞ when $r \to r_\infty$. This behavior is consistent with the physical constraints of Equation (14). Substituting Equation (19) into (11) yields a solution for the density ratio

$$r = r_\infty + (r_0 - r_\infty)a^{-3(\gamma_{dm}-\gamma_{de}-\eta_0)}. \tag{20}$$

Note that this expression differs from that obtained in Model 1 by the absence of the factor $(1+r_\infty)$ in the exponent. Consequently, the relaxation toward the fixed point occurs more rapidly, indicating a faster convergence to the stationary configuration as the interaction weakens during the evolution and the ratio approaches its asymptotic value r_∞. The redshift dependence of the interaction also affects the relative evolution of baryonic and dark matter. In particular, the ratio between their energy densities is given by

$$\frac{\rho_b(a)}{\rho_{dm}(a)} = \frac{\Omega_{b_0}}{\Omega_{de_0}} \frac{a^{-3(1-\gamma_{de}+F_\infty)}}{\left(\frac{1+r}{1+r_0}\right)^{\frac{r_\infty}{1+r_\infty}} \left[r_\infty + (r_0 - r_\infty)\, a^{-3(\gamma_{dm}-\gamma_{de}-\bar{\eta}_0)}\right]}\,, \tag{21}$$

which characterizes the evolution of the baryon-to-dark-matter density ratio during cosmic expansion. The Hubble parameter follows from the effective conservation Equations (6) and (8) once their solutions are substituted into the Friedmann Equation (2), yielding

$$\frac{H^2}{H_0^2} = \Omega_{de_0}(1+r)\left(\frac{1+r}{1+r_0}\right)^{\frac{r_\infty}{1+r_\infty}} a^{-3(\gamma_{de}-F_\infty)} + \Omega_{b_0}a^{-3} + \Omega_{\gamma_0}a^{-4} + \Omega_{\nu_0}a^{-4}\sqrt{1+(\frac{a}{a_{nr}})^2}, \tag{22}$$

where the third term arises directly from the redshift dependent interaction. As in the previous model, H_0, Ω_{de_0}, Ω_{γ_0}, Ω_{ν_0} and Ω_{b_0} represent the present value of the Hubble parameter and the present day density parameters of dark energy, photons, neutrinos and baryons, respectively.

3.3. Model 3

In this third scenario, the interaction function $F(r)$ is chosen to incorporate a rational dependence on the density ratio, allowing the energy exchange between dark matter and dark energy to vary more sensitively with the dynamical state of the system. As in the previous cases, the condition $\mathcal{F}(r_\infty) = 0$, the stationary solution is directly derived from Equation (11), ensuring that the asymptotic regime remains physically consistent. In this model, $F(r)$ is defined as

$$F(r) = \frac{r_\infty(r_\infty + 1)}{r(r+1)} F_\infty. \tag{23}$$

Note that this expression preserves the same stationary limit as Model 1, because evaluating it at $r = r_\infty$ yields the constant interaction F_∞. This construction is also consistent with the structural relation given in Equation (12), and the stability criterion stated in Equation (13) is satisfied, provided that the conditions in Equation (14) hold. Substituting the interaction function (23) into the evolution Equation (11) yields a solution for the density ratio that differs significantly from the power-law behavior obtained in the previous models. The resulting expression is

$$r = \sqrt{r_\infty^2 + (r_0^2 - r_\infty^2) a^{-6(\gamma_{dm} - \gamma_{de} - \bar{\eta}_0)}}, \tag{24}$$

where the approach toward the stationary value is characterized by nonlinear relaxation influenced by a quadratic dependence on the initial and asymptotic ratios. This structure can produce a transition that is either smoother or more abrupt than those in Models 1 and 2, depending on the values of r_0 and the effective barotropic combination $(\gamma_{dm} - \gamma_{de} - \bar{\eta}_0)$. The baryon-to-dark-matter density ratio is given by

$$\frac{\rho_b(a)}{\rho_{dm}(a)} = \frac{\Omega_{b_0}}{\Omega_{de_0}} \frac{a^{-3(1-\gamma_{de}+F_\infty)}}{r \left(\frac{r_\infty + r_0}{r_\infty + r}\right)^{\frac{r_\infty}{1-r_\infty^2}} \left(\frac{1+r}{1+r_\infty}\right)^{\frac{r_\infty^2}{1-r_\infty^2}}}, \tag{25}$$

showing how the nonlinear dependence of the interaction modifies the relative abundance of baryonic matter and dark matter. By using the solutions of the effective conservation Equations (8) and (6) in the Friedmann Equation (2), the Hubble parameter is obtained as

$$\begin{aligned} \frac{H^2}{H_0^2} &= \Omega_{de_0} a^{-3(\gamma_{de} - F_\infty)} \left(\frac{r_\infty + r_0}{r_\infty + r}\right)^{\frac{r_\infty}{1-r_\infty^2}} \left(\frac{1+r}{1+r_\infty}\right)^{\frac{r_\infty^2}{1-r_\infty^2}} (1+r) \\ &\quad + \Omega_{b_0} a^{-3} + \Omega_{\gamma_0} a^{-4} + \Omega_{\nu_0} a^{-4} \sqrt{1 + (\frac{a}{a_{nr}})^2}. \end{aligned} \tag{26}$$

This expression highlights the role of the rational structure of $F(r)$ in shaping the late-time expansion history. In particular, the dark sector contribution to $H(a)$ contains explicit r dependent factors, so that the expansion rate is determined jointly by the scale factor dependence and by the interaction induced dependence on the density ratio.

3.4. Analysis of the Function $F(r)$

The quantities r_∞ and F_∞ retain the same meanings as in the previous model. Accordingly, the constant interaction limit F_∞ is recovered when $r = r_\infty$. Model 1 corresponds to a constant interaction function, whereas Models 2 and 3 are constructed as rational functions of r. In what follows, the present value of the energy density ratio, $r_0 = \Omega_{dm}^0 / \Omega_{de}^0$, is

assumed to be known, and the constant parameters $(H_0, r_\infty, \gamma_{de}, \gamma_m, \eta_0)$ are inferred from observational constraints.

Figure 1 shows the redshift evolution of the interaction function, $F(z) \equiv F[r(z)]$, for the three dissipative cosmological models considered in this study, using the best-fit values for each model. Although the interaction term is originally defined as a function of the ratio $r \equiv \rho_{dm}/\rho_{de}$, its dependence on redshift arises through the dynamical solution $r(z)$, obtained from Equation (11) together with the relation $1 + z = a^{-1}$.

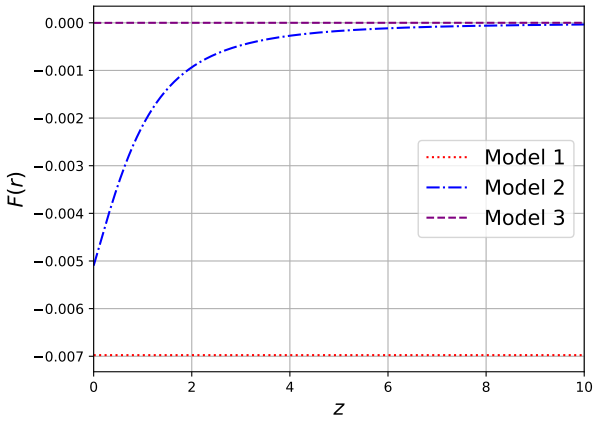


Figure 1. Redshift dependence of the interaction function $F(z) = F[r(z)]$ for the three dissipative cosmological models.

As observed, Model 1 remains constant for all redshifts, as expected, and therefore represents a genuine extension of the ΛCDM scenario in which a non-vanishing dark sector interaction is present at all cosmic epochs. In contrast, Models 2 and 3 exhibit redshift-dependent interactions. At low redshift, $F(z)$ takes negative values, whereas as the redshift increases, both models satisfy $F(z) \to 0$, thereby recovering the non-interacting ΛCDM limit ($F = 0$) at early times. In this sense, the interaction function increases toward zero as z increases (equivalently, its absolute magnitude $|F(z)|$ decreases). Although Models 2 and 3 share the same asymptotic behavior, their approaches to the early time regime are not identical. Model 3 reaches the vicinity of $F(z) \simeq 0$ faster than Model 2, displaying a steeper evolution at low and intermediate redshifts.

Figure 2 shows the redshift dependence of the ratio $r(z) \equiv \rho_{dm}/\rho_{de}$ for the three models, using the best-fit values. For redshift values in the interval $-1 \leq z \leq 0$, the three models exhibit very similar behavior, with only minor differences at $z > 0$.

To further examine the evolution of the matter sector, Figure 3 presents the redshift evolution of the dark matter-to-baryon density ratio, ρ_{dm}/ρ_b, for the three interacting dissipative models together with the reference ΛCDM cosmology. In the standard cosmological model, this ratio remains constant because both baryons and cold dark matter evolve proportionally to a^{-3}. In the present interacting scenarios, however, baryons are assumed to be independently conserved, so that $\rho_b \propto a^{-3}$ throughout the cosmic evolution, whereas the interaction with dark energy modifies the evolution of the dark matter density. Consequently, the ratio ρ_{dm}/ρ_b acquires a non-trivial redshift dependence that directly reflects the cumulative effect of the energy exchange within the dark sector.

As shown in Figure 3, Models 1 and 3 exhibit a gradual increase in the dark matter-to-baryon density ratio toward higher redshifts, whereas Model 2 displays a mild decrease over the same interval. Although all three interacting models remain within the same order of magnitude as the ΛCDM prediction throughout the explored redshift range, they retain a small but systematic deviation from the standard background evolution. This difference is already present at $z \sim 10^4$ and remains through the recombination epoch. Physically,

this behaviour arises because the interaction continuously modifies the evolution of the dark matter component, whereas baryons remain independently conserved and evolve according to the standard scaling law, $\rho_b \propto a^{-3}$. Consequently, the dark matter-to-baryon density ratio is no longer strictly constant, although the resulting departures from the standard cosmological scenario remain moderate and do not alter its overall order of magnitude. These differences indicate that the interacting models preserve a distinct background evolution with respect to ΛCDM. Nevertheless, a complete assessment of their implications for the pre-recombination acoustic physics would require solving the full system of cosmological perturbation equations within the interacting framework, which is beyond the scope of the present work.

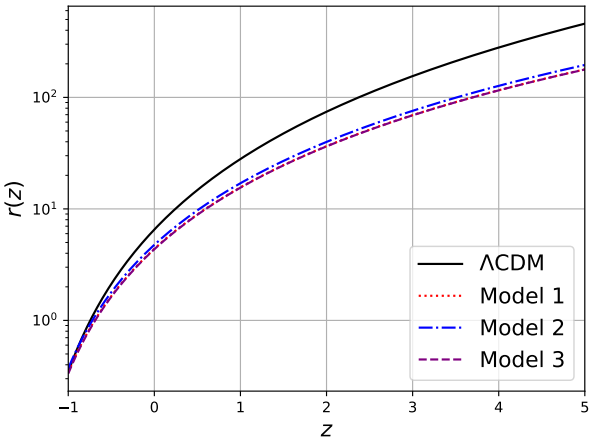


Figure 2. Evolution of the ratio $r(z) \equiv \rho_{dm}/\rho_{de}$ for the three dissipative cosmological models.

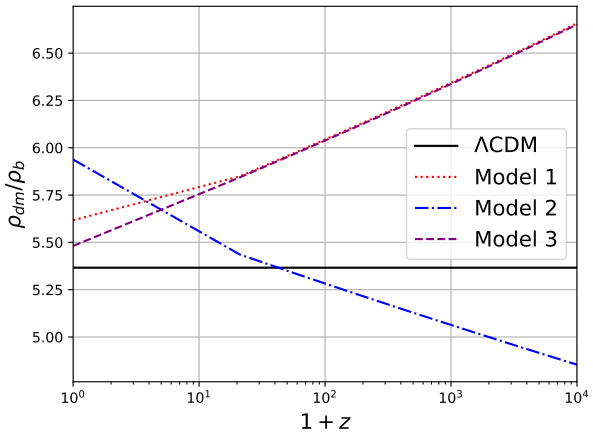


Figure 3. Evolution of the ratio ρ_{dm}/ρ_b for the three dissipative cosmological models.

4. Statistical Analysis and Observational Constraints

The datasets used in this study are described below. Different samples are considered, and a joint analysis is performed to place constraints on the cosmological parameters. The statistical analysis is based on a Bayesian approach, in which the inference of cosmological parameters $\boldsymbol{\theta}$ is obtained from the likelihood function $\mathcal{L}(D|\boldsymbol{\theta})$, where D represents the set of observational data considered. The general likelihood function can be written as

$$\mathcal{L}(D|\boldsymbol{\theta}) \propto \exp\left[-\frac{1}{2}\chi^2(\boldsymbol{\theta})\right], \tag{27}$$

where $\chi^2(\boldsymbol{\theta})$ is the chi-square statistical function associated with each data set.

4.1. Model Comparison

In order to compare the proposed models, it is necessary to calculate the Bayesian evidence, $\mathcal{E}$, for each model. The Bayesian evidence is defined as

$$\mathcal{E} = \int \mathcal{L}(\boldsymbol{\theta})\pi(\boldsymbol{\theta})d\boldsymbol{\theta}\,, \tag{28}$$

where $\mathcal{L}(\boldsymbol{\theta})$ is the likelihood function and $\pi(\boldsymbol{\theta})$ is the prior distribution of the cosmological parameters $\boldsymbol{\theta}$. For simplicity, the logarithm of the Bayesian evidence, $\ln \mathcal{E}$, is estimated from posterior samples MCMC. The comparison between two models i and j is performed calculating the Bayes factor,

$$\mathcal{B}_{ij} = \frac{\mathcal{E}_i}{\mathcal{E}_j}\,, \tag{29}$$

or equivalently,

$$\ln \mathcal{B}_{ij} = \ln \mathcal{E}_i - \ln \mathcal{E}_j\,. \tag{30}$$

The interpretation of the evidence is performed via the Jeffreys scale (see Table 1).

Table 1. Jeffreys' scale for evidence interpretation.

	Jeffreys' Scale	**Interpretation**
$\ln \mathcal{B}_{ij} < 1$	Not worth more than a bare mention	inconclusive
$1 < \ln \mathcal{B}_{ij} < 2.5$	Significant	Weak
$2.5 < \ln \mathcal{B}_{ij} < 5$	Strong to very strong	Significant
$5 < \ln \mathcal{B}_{ij}$	Decisive	Strong

4.2. Observational Samples

4.2.1. Type Ia Supernovae (Pantheon+)

To constrain the free parameters of the models, the Pantheon+ compilation of SNIa data is employed [1]. This extended sample includes 1701 light curves from 1500 spectroscopically confirmed SNIa [44] and covers the redshift range $0.001 \leq z \leq 2.3$. The dataset combines supernovae from the Sloan Digital Sky Survey (SDSS-II), SuperNova Legacy Survey (SNLS), and Hubble Space Telescope (HST) samples. The observed distance modulus is modeled within the Spectral Adaptive Light curve Template (SALT2) framework [45] as

$$\mu_{SNIa} = m_B + \alpha x_1 + \beta c - M_B - \delta_{bias} + \delta_{host}, \tag{31}$$

where α and β are global nuisance parameters related to the width x_1 and color c of the light curve, respectively. The apparent magnitude m_B and the fiducial magnitude M_B of SNIa can be calibrated with absolute distance scales such as Cepheids. δ_{bias} and δ_{host} are correction terms arising from simulation biases and the host galaxy of the SNIa. However, Pantheon+ reports the corrected apparent magnitude $m_B^{corr} = m_B + \alpha x_1 - \beta c - \delta_{bias} + \delta_{host}$, such that the distance magnitude is redefined as

$$\mu_{SNIa} = m_B^{corr} - M_B\,. \tag{32}$$

It is important to note that SNIa observations do not directly provide standard candles, but instead yield a distance modulus that can be standardized. This quantity can be computed within a given cosmological model as

$$\mu(z, \boldsymbol{\theta}) = 5 \log\left(\frac{d_L(z, \boldsymbol{\theta})}{Mpc}\right) + 25\,, \tag{33}$$

where the cosmological parameters are denoted by $\boldsymbol{\theta} := \{H_0,\ \Omega_{dm_0},\ \gamma_{de},\ \gamma_{dm},\ \bar{\eta}_0,\ r_\infty\}$. The luminosity distance for the spatially flat universe is defined as

$$d_L(z,\boldsymbol{\theta}) = \frac{c(1+z)}{H_0}\int_0^z \frac{dx}{E(x,\boldsymbol{\theta})}\,, \tag{34}$$

where $E = H/H_0$. In order to compare the observational data with the theoretical models, the SNIa likelihood is constructed by analytically marginalizing over the absolute magnitude M_B. Following Ref. [46], the resulting chi-square function is given by

$$\chi^2_{SNIa} \;=\; A - \frac{B^2}{C} + \frac{\left(B/C - M_B^{R21}\right)^2}{C^{-1} + \sigma^2_{M_B}} \tag{35}$$

where

$$A \;=\; \Delta D^\dagger \cdot C^{-1}_{Panth+} \cdot \Delta D\,, \tag{36}$$
$$B \;=\; \Delta D^\dagger \cdot C^{-1}_{Panth+} \cdot V\,, \tag{37}$$
$$C \;=\; V^\dagger \cdot C^{-1}_{Panth+} \cdot V\,. \tag{38}$$

Here, M_B^{R21} and σ_{M_B} denote the local calibration prior on the absolute magnitude of Type Ia supernovae obtained from the SH0ES analysis [47]. Futhermore, $\Delta D \equiv m_B^{corr} - \mu(z,\boldsymbol{\theta})$, the vector V denotes a column vector whose components are all equal to unity, and $C_{Panth+} \equiv C_{stat}^{Panth+} + C_{syst}^{Panth+}$ represents the covariance matrix resulting from statistical and systematic uncertainties.

4.2.2. $H(z)$ Observations (Cosmic Chronometers)

In addition to SNIa standardizable candles, cosmological clocks based on time measurements of cosmic evolution are employed. The observational Hubble parameter data $H(z)$ are obtained through the differential age method [48,49], which relies on estimating the relative age difference Δt between two passively evolving galaxies that formed at the same epoch and are separated by a small redshift interval Δz. In this way, the ratio $\Delta z/\Delta t$ provides the relation

$$H(z) = -\frac{1}{1+z}\frac{dz}{dt}\,, \tag{39}$$

which allows H to be inferred at a given redshift z. However, the ratio $\Delta z/\Delta t$ is rather difficult to obtain because a good sample of galaxy populations is needed, and it also depends largely on stellar population synthesis models [50].

The measurement at $z = 0.12$ is updated by replacing the previous determination with the recent DESI Data Release 1 result reported by Wang et al. [51], namely $H(z=0.12) = 71.33 \pm 4.20$ km s^{-1} Mpc^{-1}. The final dataset therefore consists of 32 measurements spanning the redshift range $0.07 \le z \le 1.965$.

Now, the χ^2 function can be constructed as

$$\chi^2_{CC} = \sum_{i=1}^{32}\left[\frac{H_i^{\rm obs} - H(z_i,\boldsymbol{\theta})}{\sigma_i}\right]^2 \tag{40}$$

where $H_i^{\rm obs}$ and σ_i denote the observed Hubble parameter and its associated uncertainty at redshift z_i, respectively, while $H(z_i,\boldsymbol{\theta})$ corresponds to the theoretical prediction of the cosmological model.

4.2.3. Baryon Acoustic Oscillations (BAOs)

The characteristic length scale of Baryon Acoustic Oscillations (BAOs) is imprinted in the matter distribution that encodes the physics of this early phase of the universe. This small signal excess occurs at length separations of the order of 150 comoving Mpc. For the present analysis, the latest BAO measurements from the second data release of the Dark Energy Spectroscopic Instrument (DESI DR2) [52] are incorporated. This release provides high-precision measurements of large-scale structure over an unprecedented cosmological volume. The DESI DR2 dataset provides observational values of D_M/r_d, D_H/r_d, and D_V/r_d, where r_d denotes the sound horizon at the drag epoch, defined as

$$r_d = \int_{z_d}^{\infty} \frac{c_s(z)}{H(z)} dz, \tag{41}$$

where $c_s(z)$ denotes the sound speed in the photon–baryon fluid, while $z_d \approx 1600$ [4] corresponds to the redshift of the baryon drag epoch, when photons cease to efficiently drag the baryons, causing acoustic oscillations to freeze out. The transverse comoving distance (D_M), the Hubble distance (D_H) and the volume averaged distance (D_V) are defined as

$$D_M(z) = \frac{c}{H_0} \int_0^z \frac{d\tilde{z}}{E(\tilde{z})}, \tag{42}$$

$$D_H(z) = \frac{c}{H(z)}, \tag{43}$$

$$D_V(z) \equiv \left[z D_M^2(z) D_H(z) \right]^{1/3}, \tag{44}$$

so, a BAO vector can be defined as $D_z = (D_M/r_d, D_H/r_d, D_V/r_d)$.

Now, the χ^2 function for the BAO measurements can be constructed as

$$\chi^2_{BAO} = \Delta D_z^{\dagger} \cdot C_{BAO}^{-1} \cdot \Delta D_z \,, \tag{45}$$

where $\Delta D_z \equiv D_z^{(\text{DESI DR2})}(z) - D_z(z, \boldsymbol{\theta})$ and C_{BAO}^{-1} is the 13×13 inverse covariance matrix expressed in terms of the DESI DR2 data.

Finally, to constrain the models with observational data, three separate analysis were performed, including a SNIa case defined as $\chi^2_1 = \chi^2_{\text{SNIa}}$. For joint analysis 2, combined SNIa and CC data is made by $\chi^2_2 = \chi^2_{\text{SNIa}} + \chi^2_{\text{CC}}$ and joint analysis 3 combined all data SNIa, CC, and BAO defined as $\chi^2_3 = \chi^2_{\text{SNIa}} + \chi^2_{\text{CC}} + \chi^2_{\text{BAO}}$.

5. Results and Discussion

In this section, the results derived from the statistical analysis are presented. To constrain the cosmological parameters using current observational data, Bayesian inference was performed using the Python 3.12.3 packages `NumPyro`[1] and `Jax`[2] for parallel computing. For parameter inference in the three models, 2000 samples, 1900 warmup iterations, and two chains were employed. The same prior distributions were adopted for all three models. Broad uniform priors were adopted for all free parameters to avoid introducing strong external constraints into the analysis. Specifically, $H_0 \sim \mathcal{U}(60.0, 80.0)$, $\Omega_{m_0} \sim \mathcal{U}(0.2, 0.5)$, $\gamma_{de} \sim \mathcal{U}(-0.3, 0.3)$, $\gamma_{dm} \sim \mathcal{U}(0.9, 1.1)$, $\bar{\eta}_0 \sim \mathcal{U}(0.0, 0.1)$ and $r_\infty \sim \mathcal{U}(-0.06, 0.06)$ were considered. These prior ranges were chosen to encompass the physically relevant region of the parameter space while remaining sufficiently uninformative. Tables 2, 3 and 4 summarize the estimation of the best-fit values of the parameters with 1σ (68.3%) for models 1, 2, and 3, respectively, by the corresponding analysis of SNIa, SNIa + CC and joint SNIa + CC + BAO datasets.

Table 2. Best-fit parameters with 1σ (68.3%) for the Model 1 by the analysis of SNIa, SNIa + CC and SNIa + CC + BAO.

Parameters	SNIa	SNIa + CC	SNIa + CC + BAO
H_0	$72.538^{+0.824}_{-0.837}$	$71.400^{+0.853}_{-0.757}$	$71.390^{+0.834}_{-0.766}$
Ω_{dm_0}	$0.285^{+0.088}_{-0.054}$	$0.279^{+0.075}_{-0.053}$	$0.245^{+0.023}_{-0.027}$
γ_{dm}	$0.969^{+0.074}_{-0.049}$	$0.956^{+0.071}_{-0.038}$	$1.057^{+0.029}_{-0.035}$
γ_{de}	$0.156^{+0.089}_{-0.132}$	$0.156^{+0.076}_{-0.110}$	$0.128^{+0.046}_{-0.050}$
$\bar{\eta}_0$	$0.060^{+0.028}_{-0.036}$	$0.063^{+0.027}_{-0.038}$	$0.050^{+0.028}_{-0.034}$
r_∞	$0.009^{+0.035}_{-0.046}$	$0.011^{+0.034}_{-0.045}$	$0.008^{+0.036}_{-0.036}$

Table 3. Best-fit parameters with 1σ (68.3%) for the Model 2 by the analysis of SNIa, SNIa + CC and SNIa + CC + BAO.

Parameters	SNIa	SNIa + CC	SNIa + CC + BAO
H_0	$72.568^{+0.861}_{-0.870}$	$71.442^{+0.836}_{-0.831}$	$71.389^{+0.821}_{-0.762}$
Ω_{dm_0}	$0.295^{+0.095}_{-0.066}$	$0.280^{+0.088}_{-0.054}$	$0.259^{+0.023}_{-0.031}$
γ_{dm}	$0.972^{+0.069}_{-0.054}$	$0.957^{+0.057}_{-0.042}$	$1.024^{+0.051}_{-0.054}$
γ_{de}	$0.149^{+0.095}_{-0.133}$	$0.167^{+0.069}_{-0.123}$	$0.106^{+0.052}_{-0.049}$
$\bar{\eta}_0$	$0.059^{+0.028}_{-0.034}$	$0.063^{+0.026}_{-0.034}$	$0.044^{+0.035}_{-0.029}$
r_∞	$-0.007^{+0.039}_{-0.040}$	$-0.011^{+0.047}_{-0.036}$	$0.020^{+0.028}_{-0.029}$

Table 4. Best-fit parameters with 1σ (68.3%) for the Model 3 by the analysis of SNIa, SNIa + CC and SNIa + CC + BAO.

Parameters	SNIa	SNIa + CC	SNIa + CC + BAO
H_0	$72.553^{+0.918}_{-0.873}$	$71.421^{+0.819}_{-0.766}$	$71.402^{+0.854}_{-0.751}$
Ω_{dm_0}	$0.288^{+0.087}_{-0.059}$	$0.280^{+0.075}_{-0.051}$	$0.239^{+0.010}_{-0.010}$
γ_{dm}	$0.966^{+0.072}_{-0.048}$	$0.951^{+0.065}_{-0.037}$	$1.053^{+0.031}_{-0.032}$
γ_{de}	$0.159^{+0.079}_{-0.141}$	$0.152^{+0.082}_{-0.113}$	$0.134^{+0.041}_{-0.040}$
$\bar{\eta}_0$	$0.059^{+0.030}_{-0.035}$	$0.063^{+0.026}_{-0.034}$	$0.046^{+0.031}_{-0.031}$
r_∞	$0.001^{+0.043}_{-0.043}$	$-0.002^{+0.039}_{-0.039}$	$0.001^{+0.042}_{-0.043}$

In Figure 4, the marginalized one-dimensional distributions are shown alongside the 2D posterior contours for Model 1, with the 1σ and 2σ confidence levels indicated. The SNIa-only analysis yields $H_0 = 72.538^{+0.824}_{-0.837}$ with a relatively small uncertainty, indicating that the SNIa data alone already provide a robust constraint on the present expansion rate. In contrast, the dark matter density parameter, $\Omega_{dm0} = 0.285^{+0.088}_{-0.054}$, remains only moderately constrained, reflecting the limited sensitivity of the SNIa dataset to the matter content of the Universe and the presence of parameter degeneracies, as also illustrated by the posterior contours in Figure 4. The dark matter barotropic index remains compatible with the pressureless matter limit, $\gamma_{dm} = 0.969^{+0.074}_{-0.049}$. In contrast, the dark energy barotropic index is constrained to $\gamma_{de} = 0.156^{+0.089}_{-0.132}$, with its 1σ credible interval excluding the standard zero value, indicating a departure from the ΛCDM model. The parameter $\bar{\eta}_0$ presents broad uncertainties, whereas r_∞ remains small, indicating weak constraints in the asymptotic limit (see Table 2). For the joint SNIa + CC analysis, the Hubble constant is constrained

to $H_0 = 71.400^{+0.853}_{-0.757}$, a value lower than that inferred from the SNIa-only analysis but still statistically compatible within the corresponding uncertainties. The dark matter density parameter is tightly constrained to $\Omega_{dm} = 0.279^{+0.075}_{-0.053}$. Moreover, the parameter $\gamma_{dm} = 0.956^{+0.071}_{-0.038}$ continues to be compatible with the pressureless matter limit, and $\gamma_{de} = 0.156^{+0.076}_{-0.110}$ remains shifted toward positive values. Similarly, $\bar{\eta}_0 = 0.063^{+0.027}_{-0.038}$ and $r_\infty = 0.011^{+0.034}_{-0.045}$ still exhibit broad uncertainties, indicating that the SNIa + CC combination does not yet strongly constrain the viscous and asymptotic sectors. The joint SNIa + CC + BAO analysis provides the most restrictive constraints for Model 1. In this case, the Hubble constant is constrained to $H_0 = 71.390^{+0.834}_{-0.766}$, while the dark matter density parameter decreases to $\Omega_{dm0} = 0.245^{+0.023}_{-0.027}$, showing the constraining impact of BAO measurements on the matter sector. The dark matter barotropic index shifts to $\gamma_{dm} = 1.057^{+0.029}_{-0.035}$, remaining close to the standard pressureless value but with a slight preference for values above unity. The dark energy barotropic index becomes $\gamma_{de} = 0.128^{+0.046}_{-0.050}$, still favoring positive values, although with reduced uncertainty. Finally, the parameters $\bar{\eta}_0 = 0.050^{+0.028}_{-0.034}$ and $r_\infty = 0.008^{+0.036}_{-0.036}$ remain compatible with small values, suggesting that the current data allow only weak evidence for sizable viscous or asymptotic deviations in Model 1 (see Figure 4).

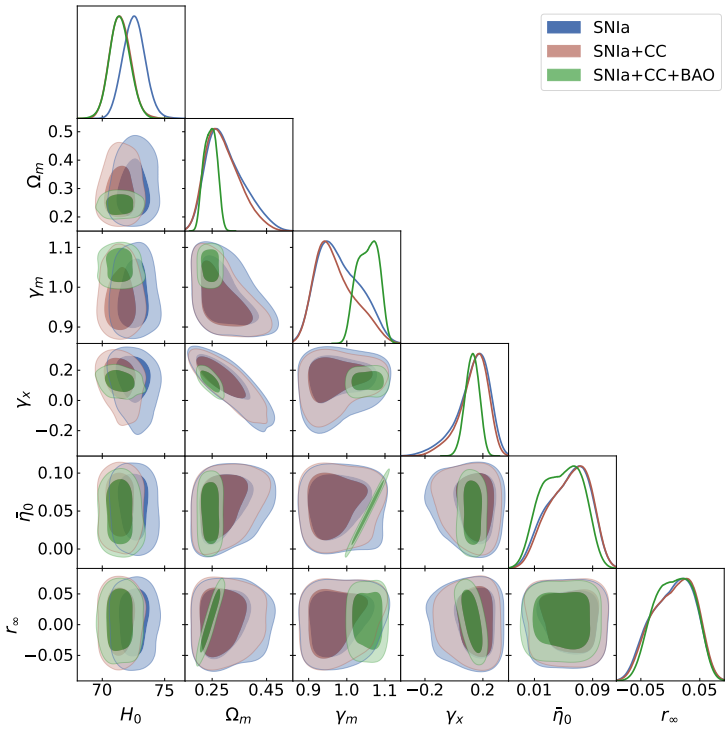


Figure 4. One-dimensional marginalized posterior distributions together with the corresponding two-dimensional posterior contours at the 1σ and 2σ confidence levels for the cosmological parameters of Model 1 obtained from the SNIa (blue), SNIa + CC (red), and SNIa + CC + BAO (green) analyses.

For Model 2, in the Figure 5 presents the marginalized one-dimensional posterior distributions together with the corresponding two-dimensional confidence contours at the 1σ and 2σ confidence levels for the analyses based on the SNIa, SNIa + CC, and SNIa + CC + BAO datasets. As in Model 1, the SNIa-only analysis provides a relatively precise estimate of the Hubble constant, $H_0 = 72.568^{+0.861}_{-0.870}$, whereas the dark matter density parameter remains more weakly constrained, with $\Omega_{dm0} = 0.295^{+0.095}_{-0.066}$. The dark matter barotropic index, $\gamma_{dm} = 0.972^{+0.069}_{-0.054}$, remains close to the pressureless matter limit, while the dark energy barotropic index, $\gamma_{de} = 0.149^{+0.095}_{-0.133}$, shows a preference for positive values within the interacting dissipative scenario. Likewise, the parameters $\bar{\eta}_0 = 0.059^{+0.028}_{-0.034}$

and $r_\infty = -0.007^{+0.039}_{-0.040}$ remain weakly constrained, as reflected by their broad posterior distributions, presents a small negative value. After incorporating the CC measurements, the Hubble constant decreases to $H_0 = 71.442^{+0.836}_{-0.831}$, while the dark matter density parameter becomes $\Omega_{dm0} = 0.280^{+0.088}_{-0.054}$, indicating a moderate improvement in the parameter constraints. The dark matter barotropic index remains close to unity, $\gamma_{dm} = 0.957^{+0.057}_{-0.042}$, whereas the dark energy barotropic index, $\gamma_{\rm de} = 0.167^{+0.069}_{-0.123}$, continues to favor positive values. The bulk-viscosity parameter, $\bar{\eta}_0 = 0.063^{+0.026}_{-0.034}$, remains broadly distributed, while $r_\infty = -0.011^{+0.047}_{-0.036}$ stays close to zero, indicating that the SNIa + CC dataset alone still provides only weak constraints on the asymptotic behavior of the interacting dark sector. Moreover, the joint SNIa + CC + BAO analysis provides the most restrictive constraints for Model 2. In this case, the Hubble constant is estimated as $H_0 = 71.389^{+0.821}_{-0.762}$, whereas the dark matter density parameter decreases to $\Omega_{dm0} = 0.259^{+0.023}_{-0.031}$, showing the constraining effect of the BAO observations on the matter sector. The dark matter barotropic index shifts to $\gamma_{dm} = 1.024^{+0.051}_{-0.054}$ while remaining close to the pressureless matter limit, whereas the dark energy barotropic index becomes $\gamma_{de} = 0.106^{+0.052}_{-0.049}$ with a noticeably reduced uncertainty. Likewise, the bulk-viscosity parameter decreases to $\bar{\eta}_0 = 0.044^{+0.035}_{-0.029}$, while $r_\infty = 0.020^{+0.028}_{-0.029}$ remains compatible with values close to zero. Overall, Figure 5 and Table 3 show that incorporating BAO measurements significantly tightens the posterior distributions and reduces the remaining parameter degeneracies for Model 2.

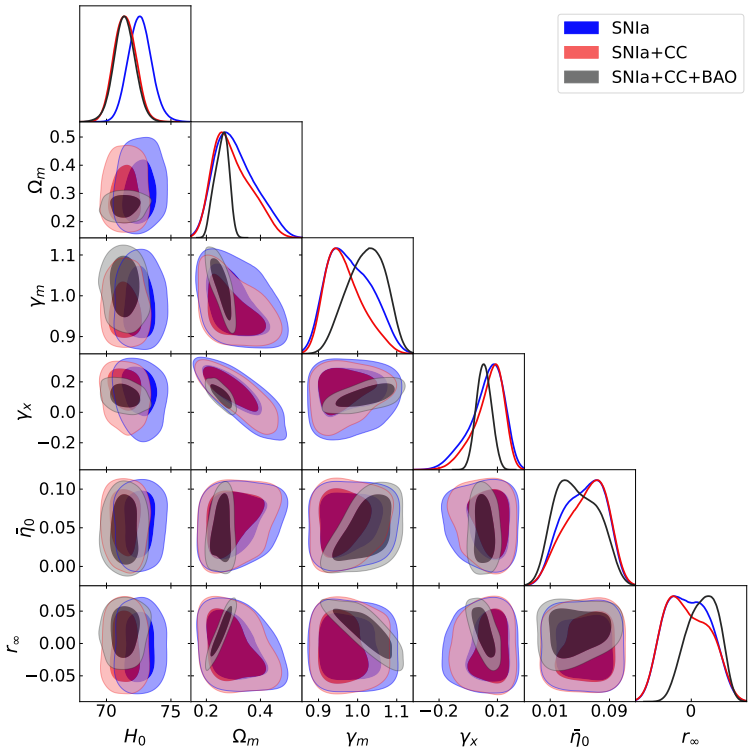


Figure 5. One-dimensional marginalized posterior distributions together with the corresponding two-dimensional posterior contours at the 1σ and 2σ confidence levels for the cosmological parameters of Model 2 obtained from the SNIa (blue), SNIa + CC (red), and SNIa + CC + BAO (gray) analyses.

Figure 6 presents the marginalized one-dimensional posterior distributions together with the corresponding two-dimensional confidence contours at the 1σ and 2σ confidence levels for Model 3 using the SNIa, SNIa + CC, and SNIa + CC + BAO datasets. As in the previous models, the incorporation of complementary observational probes progressively reduces the posterior volume and improves the constraints on the cosmological parameters. Compared with Models 1 and 2, Model 3 exhibits a slightly different posterior structure, particularly for the dark-sector parameters, while preserving the same overall

cosmological behavior. In Table 4, for the SNIa + CC analysis, the Hubble constant is constrained to $H_0 = 71.421^{+0.819}_{-0.766}$, while the present dark matter density is $\Omega_{dm0} = 0.280^{+0.075}_{-0.051}$. The dark matter barotropic index remains close to the pressureless matter limit, with $\gamma_{dm} = 0.951^{+0.065}_{-0.037}$, whereas the dark energy barotropic index, $\gamma_{de} = 0.152^{+0.082}_{-0.113}$, continues to favor positive values within the interacting dissipative scenario. The bulk-viscosity parameter, $\bar{\eta}_0 = 0.063^{+0.026}_{-0.034}$, together with $r_\infty = -0.002^{+0.039}_{-0.039}$, remains only weakly constrained, consistently with the broad posterior distributions shown in Figure 6. After incorporating the BAO measurements into the joint analysis, the constraints become significantly tighter. The Hubble constant is estimated as $H_0 = 71.402^{+0.854}_{-0.751}$, whereas the dark matter density decreases to $\Omega_{dm0} = 0.239^{+0.010}_{-0.010}$, reflecting the strong constraining power of BAO on the matter sector. The dark matter barotropic index shifts to $\gamma_{dm} = 1.053^{+0.031}_{-0.032}$, while the dark energy barotropic index becomes $\gamma_{de} = 0.134^{+0.041}_{-0.040}$ with substantially reduced uncertainties. Likewise, the bulk-viscosity parameter decreases to $\bar{\eta}_0 = 0.046^{+0.031}_{-0.031}$, whereas $r_\infty = 0.001^{+0.042}_{-0.043}$ remains fully compatible with zero. Overall, the SNIa + CC + BAO analysis provides the most restrictive constraints for Model 3. In particular, the matter density parameter exhibits the largest improvement with respect to the SNIa-only analysis, while the posterior distributions of the dark-sector parameters become noticeably narrower. Nevertheless, the parameter r_∞ remains centered around zero, indicating that the current observational data still provide only limited information on the asymptotic behavior of the interacting dark sector.

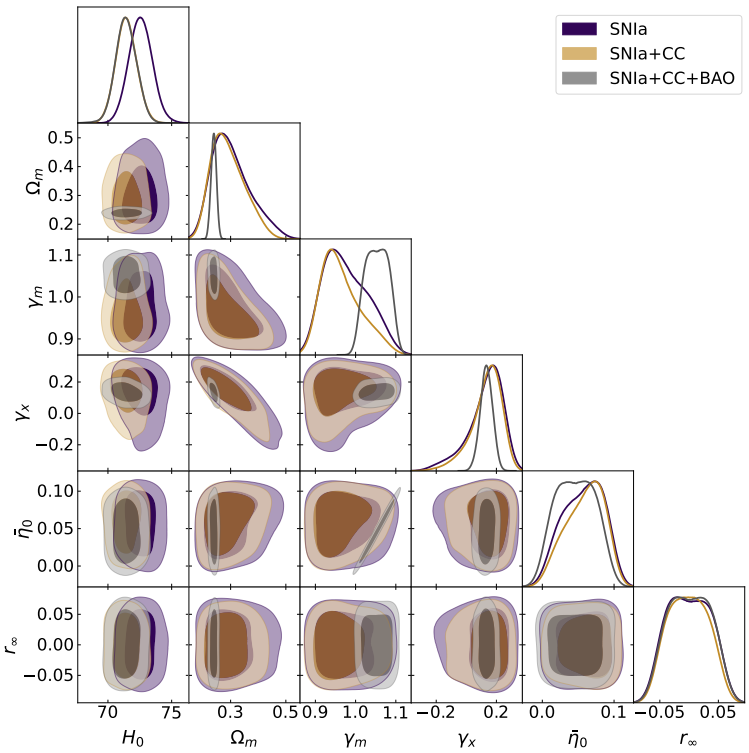


Figure 6. One-dimensional marginalized distribution, and the 2D posterior contours with 1σ and 2σ Confidence Levels for the cosmological parameters of the model 3 by the analysis of SNIa (purple), SNIa + CC (gold) and SNIa + CC + BAO (gray).

To compare the proposed cosmological scenarios with the reference ΛCDM model, the Bayesian evidence was computed for each model using the joint SNIa + CC + BAO analysis, and the corresponding Bayes factors were evaluated with respect to the reference model (see Table 5). The three interacting dissipative models exhibit Bayesian evidences very close to that of the ΛCDM model, yielding $|\ln B_{01}| = 0.555$, $|\ln B_{02}| = 0.002$, and $|\ln B_{03}| = 0.489$. According to the Jeffreys scale presented in Table 1, these values fall

within the inconclusive evidence region, indicating that the current observational data do not provide statistically significant Bayesian evidence either in favor of or against the interacting dissipative models relative to the standard ΛCDM scenario. Nevertheless, the Bayesian evidence already accounts for the larger parameter space of the proposed models through the intrinsic Occam's razor penalty, making these results particularly relevant because the alternative scenarios contain four additional free parameters with respect to the reference ΛCDM model.

Table 5. Model comparison via Bayes factor.

Model	$\ln \mathcal{E}$	$\lvert \ln \mathcal{B} \rvert$	Interpretation
ΛCDM	−904.209	0	–
Model 1	−903.654	0.555	Inconclusive evidence
Model 2	−904.207	0.002	Inconclusive evidence
Model 3	−903.720	0.489	Inconclusive evidence

6. Conclusions

In this study, three interacting dark-sector models were constructed, incorporating the bulk viscosity as a dissipative contribution to the cosmic fluid. Model 1 was defined by a constant interaction term $F(r) = F_\infty$, corresponding to a fixed asymptotic value selected by the stationary condition. Model 2 was given by $F(r) = \frac{1+r_\infty}{1+r} F_\infty$, while Model 3 was defined as $F(r) = \frac{r_\infty(r_\infty+1)}{r(r+1)} F_\infty$. Models 2 and 3 were constructed to maintain the same stationary limit as Model 1. Within a dynamical system framework, we derived the evolution equation for r and established conditions that ensure dynamical stability and consistent late-time behavior. Moreover, the analysis of the dark matter-to-baryon density ratio shows that the interaction modifies the background evolution of the dark matter component, leading to a moderate redshift dependence that distinguishes the proposed interacting scenarios from the standard ΛCDM cosmology. Although a small residual deviation persists up to the pre-recombination epoch, the ratio remains close to the standard prediction throughout the explored redshift range. These results indicate that the interaction does not produce extreme departures in the early-time matter composition, but rather introduces moderate modifications to the background evolution while preserving the overall behaviour of the cosmological matter sector. The three interacting dark-sector models were subsequently confronted with the SNIa, SNIa + CC, and SNIa + CC + BAO observational datasets in order to constrain their parameter space. The adoption of broad and uninformative priors allowed the physically relevant region of the parameter space to be explored without introducing external biases into the Bayesian inference. Overall, the three interaction prescriptions provide a consistent description of the current observational data and exhibit the same qualitative cosmological behavior. As progressively more observational information is incorporated, particularly through the addition of BAO measurements, the constraints become noticeably tighter, leading to a substantial reduction in the uncertainties associated with the present dark matter density, while the viscosity parameter and the asymptotic ratio remain only weakly constrained.

An important outcome of this work is the complementary role played by the different observational probes in constraining the interacting dark-sector models. While the SNIa dataset alone already provides a relatively precise determination of the Hubble constant, the inclusion of Cosmic Chronometers and, especially, BAO measurements substantially improves the constraints on the matter sector, leading to a significant reduction in the uncertainty of the present dark matter density parameter. This progressive improvement is consistently observed for the three interaction prescriptions, highlighting the importance

of combining independent cosmological observations to reduce parameter degeneracies. Regarding the physical properties of the models, the dark matter barotropic index remains close to the pressureless limit in all three scenarios, indicating that neither the interaction nor the bulk-viscous contribution significantly modifies the effective behavior of dark matter. In contrast, the dark energy barotropic index systematically favors positive values, although its posterior distribution becomes progressively narrower as additional observational datasets are incorporated. Likewise, the bulk-viscosity parameter remains constrained to small positive values, whereas the asymptotic ratio parameter is consistently compatible with values close to zero. Consequently, although the current observations do not provide compelling evidence for sizeable dissipative effects, they also do not exclude their presence within the dark sector. Overall, the three interaction models exhibit remarkably similar cosmological behavior despite their different interaction functions. The differences among them are mainly quantitative rather than qualitative, with Model 3 providing slightly tighter constraints for some dark-sector parameters without leading to a substantially different cosmological interpretation. This overall consistency suggests that the stationary-condition approach adopted to construct the interaction functions constitutes a robust and physically consistent framework for describing the late-time evolution of the dark sector. Finally, the Bayesian model comparison indicates that the three interacting dissipative models yield Bayesian evidence values very close to that of the reference ΛCDM cosmology. According to the Jeffreys scale, the resulting Bayes factors correspond to inconclusive evidence, indicating that the current observational data do not provide sufficient statistical support either in favor of or against the proposed interacting scenarios. Nevertheless, this result is particularly meaningful because the Bayesian evidence naturally incorporates the Occam penalty associated with the four additional free parameters of the interacting models. Therefore, although the present observations do not statistically favor these extensions over the standard cosmological model, neither do they exclude them, leaving interacting viscous cosmologies as viable alternatives that should be reassessed with future high-precision cosmological observations.

Author Contributions: Conceptualization, C.Z.V. and W.C.A.; methodology, C.Z.V., W.C.A. and A.E.O.; software, C.Z.V.; validation, C.Z.V.; formal analysis, C.Z.V., W.C.A., A.E.O. and A.G.J.; writing—original draft preparation, A.E.O.; writing—review and editing, C.Z.V., W.C.A., A.E.O. and A.G.J. All authors have read and agreed to the published version of the manuscript.

Funding: This research received funding from the National Council for Science, Technology, and Technological Innovation (CONCYTEC), the National Program for Scientific Research and Advanced Studies (PROCIENCIA), and Universidad Tecnológica del Perú (UTP), within the framework of the competition E041-2024-03 Basic Research Projects, grant number PE501088539-2024. The APC was funded by CONCYTEC and PROCIENCIA.

Data Availability Statement: The original contributions presented in this study are included in the article.

Acknowledgments: The authors acknowledge the financial support provided by PROCIENCIA and the Universidad Tecnológica del Perú for the development of this research. The authors also thank to anonymous referee for the rigorous review, which helped improve the quality of the manuscript.

Conflicts of Interest: The authors declare no conflicts of interest.

Notes

[1] https://num.pyro.ai/en/stable/ (accessed on 12 July 2026).
[2] https://docs.jax.dev/en/latest/index.html (accessed on 12 July 2026).

References

1. Brout, D.; Scolnic, D.; Popovic, B.; Riess, A.G.; Carr, A.; Zuntz, J.; Kessler, R.; Davis, T.M.; Hinton, S.; Jones, D.; et al. The Pantheon+ Analysis: Cosmological Constraints. *Astrophys. J.* **2022**, *938*, 110. [CrossRef]
2. Riess, A.G.; Filippenko, A.V.; Challis, P.; Clocchiatti, A.; Diercks, A.; Garnavich, P.M.; Gilliland, R.L.; Hogan, C.J.; Jha, S.; Kirshner, R.P.; et al. Observational Evidence from Supernovae for an Accelerating Universe and a Cosmological Constant. *Astron. J.* **1998**, *116*, 1009–1038. [CrossRef]
3. Perlmutter, S.; Aldering, G.; Goldhaber, G.; Knop, R.A.; Nugent, P.; Castro, P.G.; Deustua, S.; Fabbro, S.; Goobar, A.; Groom, D.E.; et al. Measurements of Ω and Λ from 42 High-Redshift Supernovae. *Astrophys. J.* **1999**, *517*, 565–586. [CrossRef]
4. Aghanim, N. et al. [Planck Collaboration] Planck 2018 results—VI. Cosmological parameters. *Astron. Astrophys.* **2020**, *641*, A6. [CrossRef]
5. Di Valentino, E.; Mena, O.; Pan, S.; Visinelli, L.; Yang, W.; Melchiorri, A.; Mota, D.F.; Riess, A.G.; Silk, J. In the realm of the Hubble tension—A review of solutions. *Class. Quantum Gravity* **2021**, *38*, 153001. [CrossRef]
6. Riess, A.G.; Yuan, W.; Macri, L.M.; Scolnic, D.; Brout, D.; Casertano, S.; Jones, D.O.; Murakami, Y.; Anand, G.S.; Breuval, L.; et al. A Comprehensive Measurement of the Local Value of the Hubble Constant with 1 km s-1 Mpc-1 Uncertainty from the Hubble Space Telescope and the SH0ES Team. *Astrophys. J. Lett.* **2022**, *934*, L7. [CrossRef]
7. Camarena, D.; Marra, V. Local determination of the Hubble constant and the deceleration parameter. *Phys. Rev. Res.* **2020**, *2*, 013028. [CrossRef]
8. Valentino, E.D.; Said, J.L.; Riess, A.; Pollo, A.; Poulin, V.; Gómez-Valent, A.; Weltman, A.; Palmese, A.; Huang, C.D.; van de Bruck, C.; et al. The CosmoVerse White Paper: Addressing observational tensions in cosmology with systematics and fundamental physics. *Phys. Dark Universe* **2025**, *49*, 101965. [CrossRef]
9. Casertano, S.; Anand, G.; Anderson, R.I.; Beaton, R.; Bhardwaj, A.; Blakeslee, J.P.; Boubel, P.; Breuval, L.; Brout, D.; Cantiello, M.; et al. The Local Distance Network: A community consensus report on the measurement of the Hubble constant at ∼1% precision. *Astron. Astrophys.* **2026**, *708*, A166. [CrossRef]
10. Moresco, M.; Pozzetti, L.; Cimatti, A.; Jimenez, R.; Maraston, C.; Verde, L.; Thomas, D.; Citro, A.; Tojeiro, R.; Wilkinson, D. A 6% measurement of the Hubble parameter at z 0.45: Direct evidence of the epoch of cosmic re-acceleration. *J. Cosmol. Astropart. Phys.* **2016**, *2016*, 014. [CrossRef]
11. Alam, S.; Aubert, M.; Avila, S.; Balland, C.; Bautista, J.E.; Bershady, M.A.; Bizyaev, D.; Blanton, M.R.; Bolton, A.S.; Bovy, J.; et al. Completed SDSS-IV extended Baryon Oscillation Spectroscopic Survey: Cosmological implications from two decades of spectroscopic surveys at the Apache Point Observatory. *Phys. Rev. D* **2021**, *103*, 083533. [CrossRef]
12. Guo, W.; Wang, Q.; Cao, S.; Biesiada, M.; Liu, T.; Lian, Y.; Jiang, X.; Mu, C.; Cheng, D. Newest Measurements of Hubble Constant from DESI 2024 Baryon Acoustic Oscillation Observations. *Astrophys. J. Lett.* **2025**, *978*, L33. [CrossRef]
13. Cogato, F.; Moresco, M.; Amati, L.; Cimatti, A. An analytical late–Universe approach to the weaving of modern cosmology. *Mon. Not. R. Astron. Soc.* **2023**, *527*, 4874–4888. [CrossRef]
14. Kumar, S.; Nunes, R.C. Probing the interaction between dark matter and dark energy in the presence of massive neutrinos. *Phys. Rev. D* **2016**, *94*, 123511. [CrossRef]
15. Jesus, J.F.; Escobal, A.A.; Benndorf, D.; Pereira, S.H. Can dark matter–dark energy interaction alleviate the cosmic coincidence problem? *Eur. Phys. J. C* **2022**, *82*, 273. [CrossRef]
16. Pan, S.; Yang, W.; Di Valentino, E.; Saridakis, E.N.; Chakraborty, S. Interacting scenarios with dynamical dark energy: Observational constraints and alleviation of the H_0 tension. *Phys. Rev. D* **2019**, *100*, 103520. [CrossRef]
17. Khyllep, W.; Dutta, J.; Basilakos, S.; Saridakis, E.N. Background evolution and growth of structures in interacting dark energy scenarios through dynamical system analysis. *Phys. Rev. D* **2022**, *105*, 043511. [CrossRef]
18. Benisty, D.; Pan, S.; Staicova, D.; Di Valentino, E.; Nunes, R.C. Late-time constraints on interacting dark energy: Analysis independent of H_0, rd, and MB. *Astron. Astrophys.* **2024**, *688*, A156. [CrossRef]
19. D'Agostino, R.; Nunes, R.C. Measurements of H_0 in modified gravity theories: The role of lensed quasars in the late-time Universe. *Phys. Rev. D* **2020**, *101*, 103505. [CrossRef]
20. Vargas, C.Z.; Hipólito-Ricaldi, W.S.; Zimdahl, W. Perturbations for transient acceleration. *J. Cosmol. Astropart. Phys.* **2012**. [CrossRef]
21. An, R.; Feng, C.; Wang, B. Relieving the tension between weak lensing and cosmic microwave background with interacting dark matter and dark energy models. *J. Cosmol. Astropart. Phys.* **2018**, *2018*, 038. [CrossRef]
22. Brevik, I.; Normann, B.D. Remarks on Cosmological Bulk Viscosity in Different Epochs. *Symmetry* **2020**, *12*, 1085. [CrossRef]
23. Cruz, N.; González, E.; Palma, G. Exact analytical solution for an Israel–Stewart cosmology. *Gen. Relativ. Gravit.* **2020**, *52*, 62. [CrossRef]
24. Tamayo, D. Thermodynamics of viscous dark energy for the late future time universe. *Rev. Mex. Física* **2022**, *68*, 1–12. [CrossRef]
25. Elkhateeb, E.A.; Hashim, M. Dissipative unified dark fluid: Observational constraints. *J. High Energy Astrophys.* **2023**, *37*, 3–14. [CrossRef]

26. Mandal, S.; Parida, A.; Sahoo, P.K. Observational Constraints and Some Toy Models in f(Q) Gravity with Bulk Viscous Fluid. *Universe* **2022**, *8*, 240. [CrossRef]
27. Dixit, A.; Pradhan, A. Bulk viscous flat FLRW model with observational constraints in f (T, B) gravity. *Universe* **2022**, *8*, 650. [CrossRef]
28. Kremer, G.M.; Sobreiro, O.A. Bulk viscous cosmological model with interacting dark fluids. *Braz. J. Phys.* **2012**, *42*, 77–83. [CrossRef]
29. Chimento, L.P.; Forte, M.; Kremer, G.M. Cosmological model with interactions in the dark sector. *Gen. Relativ. Gravit.* **2009**, *41*, 1125–1137. [CrossRef]
30. Di Valentino, E.; Melchiorri, A.; Mena, O.; Vagnozzi, S. Interacting dark energy in the early 2020s: A promising solution to the H_0 and cosmic shear tensions. *Phys. Dark Universe* **2020**, *30*, 100666. [CrossRef]
31. Di Valentino, E.; Melchiorri, A.; Mena, O.; Vagnozzi, S. Nonminimal dark sector physics and cosmological tensions. *Phys. Rev. D* **2020**, *101*, 063502. [CrossRef]
32. Yang, W.; Di Valentino, E.; Pan, S.; Wu, Y.; Lu, J. Dynamical dark energy after Planck CMB final release and H_0 tension. *Mon. Not. R. Astron. Soc.* **2020**, *501*, 5845–5858. [CrossRef]
33. Solà Peracaula, J.; Gómez-Valent, A.; de Cruz Pérez, J.; Moreno-Pulido, C. Running Vacuum in the Universe: Phenomenological Status in Light of the Latest Observations, and Its Impact on the σ_8 and H_0 Tensions. *Universe* **2023**, *9*, 262. [CrossRef]
34. Montani, G.; Carlevaro, N.; Dainotti, M. Running Hubble constant: Evolutionary Dark Energy. *Phys. Dark Universe* **2025**, *48*, 101847. [CrossRef]
35. Moresco, M.; Amati, L.; Amendola, L.; Birrer, S.; Blakeslee, J.P.; Cantiello, M.; Cimatti, A.; Darling, J.; Valle, M.D.; Fishbach, M.; et al. Unveiling the Universe with emerging cosmological probes. *Living Rev. Relativ.* **2022**, *25*, 6. [CrossRef]
36. Favale, A.; Gomez-Valent, A.; Migliaccio, M. Cosmic chronometers to calibrate the ladders and measure the curvature of the Universe A model-independent study. *Mon. Not. R. Astron. Soc.* **2023**, *523*, 3406–3422. [CrossRef]
37. Pan, S.; Yang, W.; Paliathanasis, A. Non-linear interacting cosmological models after Planck 2018 legacy release and the H_0 tension. *Mon. Not. R. Astron. Soc.* **2020**, *493*, 3114–3131. [CrossRef]
38. Nesseris, S.; Pantazis, G.; Perivolaropoulos, L. Tension and constraints on modified gravity parametrizations of Geff(z) from growth rate and Planck data. *Phys. Rev. D* **2017**, *96*, 023542. [CrossRef]
39. Nájera, J.A.; Banik, I.; Desmond, H.; Kalaitzidis, V. Comparing Measures of the Hubble and BAO Tensions in ΛCDM and Possible Solutions in f(Q) Gravity. *Galaxies* **2026**, *14*, 19. [CrossRef]
40. Adhikari, S.; Banerjee, A.; Jain, B.; Shin, T.H.; Zhong, Y.M. Constraints on Dark Matter Self-interactions from Weak Lensing of Galaxies from the Dark Energy Survey around Clusters from the Atacama Cosmology Telescope Survey. *Astrophys. J.* **2025**, *983*, 50. [CrossRef]
41. Shen, X.; Hopkins, P.F.; Necib, L.; Jiang, F.; Boylan-Kolchin, M.; Wetzel, A. Dissipative Dark Matter on FIRE. II. Observational Signatures and Constraints from Local Dwarf Galaxies. *Astrophys. J.* **2024**, *966*, 131. [CrossRef]
42. Khatri, V.; Singh, C.; Srivastava, M. Exploring interacting bulk viscous model with decaying vacuum density. *Astron. Comput.* **2025**, *53*, 100992. [CrossRef]
43. Bansal, P.; Johnson, J.P.; Shankaranarayanan, S. Interacting dark sector from Horndeski theories and beyond: Mapping fields and fluids. *Phys. Rev. D* **2025**, *111*, 024071. [CrossRef]
44. Scolnic, D.M.; Jones, D.; Rest, A.; Pan, Y.; Chornock, R.; Foley, R.; Huber, M.; Kessler, R.; Narayan, G.; Riess, A.; et al. The complete light-curve sample of spectroscopically confirmed SNe Ia from Pan-STARRS1 and cosmological constraints from the combined pantheon sample. *Astrophys. J.* **2018**, *859*, 101. [CrossRef]
45. Guy, J.; Astier, P.; Baumont, S.; Hardin, D.; Pain, R.; Regnault, N.; Basa, S.; Carlberg, R.G.; Conley, A.; Fabbro, S.; et al. SALT2: Using distant supernovae to improve the use of type Ia supernovae as distance indicators. *Astron. Astrophys.* **2007**, *466*, 11–21. [CrossRef]
46. Camarena, D.; Marra, V. On the use of the local prior on the absolute magnitude of Type Ia supernovae in cosmological inference. *Mon. Not. R. Astron. Soc.* **2021**, *504*, 5164–5171. [CrossRef]
47. Riess, A.G.; Casertano, S.; Yuan, W.; Bowers, J.B.; Macri, L.; Zinn, J.C.; Scolnic, D. Cosmic Distances Calibrated to 1% Precision with Gaia EDR3 Parallaxes and Hubble Space Telescope Photometry of 75 Milky Way Cepheids Confirm Tension with ΛCDM. *Astrophys. J. Lett.* **2021**, *908*, L6. [CrossRef]
48. Dunlop, J.; Peacock, J.; Spinrad, H.; Dey, A.; Jimenez, R.; Stern, D.; Windhorst, R. A 3.5-Gyr-old galaxy at redshift 1.55. *Nature* **1996**, *381*, 581–584. [CrossRef]
49. Jimenez, R.; Loeb, A. Constraining Cosmological Parameters Based on Relative Galaxy Ages. *Astrophys. J.* **2002**, *573*, 37. [CrossRef] [PubMed]
50. Moresco, M.; Cimatti, A.; Jimenez, R.; Pozzetti, L.; Zamorani, G.; Bolzonella, M.; Dunlop, J.; Lamareille, F.; Mignoli, M.; Pearce, H.; et al. Improved constraints on the expansion rate of the Universe up to z∼1.1 from the spectroscopic evolution of cosmic chronometers. *J. Cosmol. Astropart. Phys.* **2012**, *2012*, 006. [CrossRef]

51. Wang, Z.F.; Lei, L.; Fan, Y.Z. New H(z) Measurement at Redshift = 0.12 with DESI Data Release 1. *Astrophys. J.* **2026**, *1003*, 81. [CrossRef]
52. Karim, M.A. et al. [DESI Collaboration] DESI DR2 results. II. Measurements of baryon acoustic oscillations and cosmological constraints. *Phys. Rev. D* **2025**, *112*, 083515. [CrossRef]

Disclaimer/Publisher's Note: The statements, opinions and data contained in all publications are solely those of the individual author(s) and contributor(s) and not of MDPI and/or the editor(s). MDPI and/or the editor(s) disclaim responsibility for any injury to people or property resulting from any ideas, methods, instructions or products referred to in the content.